CONFERENCE PRE-PRINT

UNDERSTANDING RADIAL DENSITY FLATTENING IN THE FAR-SOL OF H-MODE PLASMAS ON JET

C. PEREZ VON THUN^{1,*}, R.B. MORALES², M. BERNERT³, L. FRASSINETTI⁴, N. VIANELLO⁵, A. BOBOC², M. FAITSCH³, M. GROTH⁶, A. HUBER⁷, D. KOS², B. LOMANOWSKI⁸, A.G. MEIGS², N. PANADERO⁹, G. SERGIENKO⁷, S.A. SILBURN², D. SILVAGNI³, G. SZEPESI², B. THOMAS², A. TOOKEY², S. ALEIFERIS¹⁰, M. BRIX², M. LENNHOLM², O. GROVER³, D. REFY¹¹, H.J. SUN², JET CONTRIBUTORS^a, AND THE EUROFUSION TOKAMAK EXPLOITATION TEAM^b

Abstract

The current understanding of density flattening and the formation of density shoulders in the far scrape-off-layer (SOL) is insufficient to be able to predict quantitatively the main chamber W source in the new full-W ITER. In the present work, electron density profiles in the far-SOL of JET tokamak H-mode plasma are carefully evaluated for a set of H-mode density ramp experiments covering a variety of conditions (different plasma triangularity, vertical vs horizontal outer target geometry, different parallel connection lengths to the divertor L_{\parallel} , or exchanging gas fuelling against pellets). Despite the dataset's heterogeneity, the edge turbulence control parameter (α_i) evaluated at the separatrix position is found to unify the radial decay of n_e in the far-SOL ($\lambda_{n,far}$) for the entire dataset, typically to within +- 25%. A direct proportionality between the two is found, both in normalised poloidal flux coordinates ($\lambda_{n,far}[\psi_N] = 0.123 * \alpha_i$) and in real space outer midplane radius ($\lambda_{n,far}[mm] = 70 * \alpha_i$). The outer inflection radius of the density shoulders seen to develop at high enough α_i (>~ 1.2) appears to be set in these pulses (with relatively large clearance to the outer wall) by the intersection of the open field lines with the LFS divertor top, rather than the limiters in the main chamber. This may offer a route to prevent direct contact of a density shoulder in ITER with the main chamber walls.

1. INTRODUCTION

With the recent decision to pursue a full-W wall for ITER [1], the W source from the main chamber poses a new risk [2]. State of the art plasma-wall-interaction simulations for ITER, using different combinations of n_e & T_i reached in front of the main chamber tiles as input, show that W sputtering from the main chamber could far outweigh other W sources [3,4]. The combination of high n_e and high T_i is the 'worst case scenario', yielding the highest W source. However, at present there is no reliable prediction for what n_e & T_i at that location in ITER will be. In order to constrain these simulations for ITER, it has become critical to advance the physics basis to extrapolate far-SOL profile measurements from current machines to ITER with sufficient accuracy. This includes a better comprehension of the physics governing SOL density flattening and the formation of density shoulders, e.g. [5].

During its final year of operation, a new set of H-mode fuelling ramp experiments was implemented on JET. Density was ramped from medium densities (Greenwald fraction $f_{GW} \sim 0.6$ -0.7) all the way up to the maximum sustainable H-mode density (H-mode density limit, or HDL, $f_{GW} \sim 1$), while the electron densities at the separatrix location ($n_{e,sep}$) were pushed from typically $n_{e,sep}/n_{GW} \sim 0.25$ -0.35 up to 0.5-0.65. A fuelling ramp

^aSee the author list of "Overview of T and D-T results in JET with ITER-like wall" by CF Maggi et al. Nuclear Fusion 64 (2024) 112012, DOI: 10.1088/1741-4326/ad3e16

^bSee the author list of "Overview of the EUROfusion Tokamak Exploitation programme in support of ITER and DEMO" by E. Joffrin Nuclear Fusion 2024 10.1088/1741-4326/ad2be4

¹Institute of Plasma Physics and Laser Microfusion, Warsaw, Poland.

²UKAEA, Culham Science Centre, Abingdon, United Kingdom of Great Britain and Northern Ireland.

³Max Planck Institute for Plasma Physics, Garching, Germany.

⁴Fusion Plasma Physics, KTH, Stockholm, Sweden.

⁵Consorzio RFX, Padova, Italy.

⁶Aalto University, Aalto, Finland.

⁷Forschungszentrum Jülich GmbH, Institute of Fusion Energy and Nuclear Waste Management, Jülich, Germany.

⁸Oak Ridge National Laboratory, Oak Ridge, United States of America.

⁹National Fusion Laboratory, CIEMAT, Madrid, Spain.

¹⁰NCSR 'Demokritos', Agia Paraskevi Attikis, Greece.

¹¹Centre for Energy Research, Budapest, Hungary.

^{*}Email: christian.perez.von.thun@ifpilm.pl

example is shown in figure 1. By repeating these fuelling ramps for different target plasmas or with different fuelling techniques (pellets or gas), a highly diverse set of near- and far-SOL profiles for H-modes was compiled. Individual discharge pairs were generated (including different plasma shaping, outer target geometry, or parallel connection length to the divertor L_{\parallel}), that will be used here to help identify which are the key drivers for density flattening and density shoulder formation, and what determines the radial extent of the density shoulder.

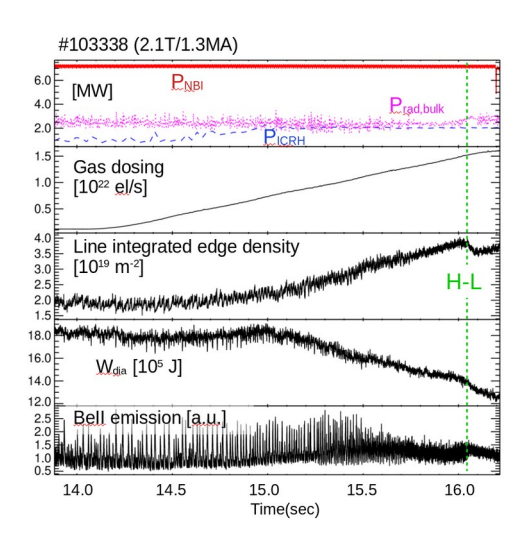


FIG. 1. Selection of timetraces for a (gas driven) density ramp up to the maximum sustainable H-mode density (H-L). Other parameters for this discharge are: B_{tor} =2.1T, I_p =1.3MA, q_{95} =5.7, $L_{||}$ = 48m, low triangularity ($<\delta>\sim$ 0.27) and OSP on horizontal target.

The scenarios were designed to take advantage of the latest diagnostic improvements on JET, including the FM-CW reflectometer diagnostic [6]. The very high time and spatial resolution of the FM-CW reflectometer has enabled main chamber SOL density measurements with unprecedented detail on JET. To further improve the absolute radial positioning (with mm accuracy), new additional crosschecks against a 'triangle' of measurements consisting of the Far-Infrared (FIR) Interferometer [7,8] and the High Resolution Thomson Scattering (HRTS) [9,10] diagnostics have been included in the reflectometry evaluation workflow for this work. An example of resulting profiles is shown in figure 2. The radial positioning of each reflectometry profile is constrained with the line-integrated measurement from the interferometry through the LFS edge. The absolute position of the HRTS density profile (and the value of $T_{e,sep}$) is determined iteratively through power balance as in [11], assuming dominant Spitzer-Härm electron heat condution. The level of consistency obtained between the resulting average reflectometry profiles and the HRTS density datapoints is then used to estimate the corresponding error bars.

The upstream profile measurements were complemented with good diagnostic coverage in the divertor. The spatially averaged (around the outer strike point) temperature at the outer target location ($T_{e,OT}$) has been inferred from Balmer photo-recombination continuum emission [12,13]. Electron densities around the outer strike point ($n_{e,OT}$) have been inferred from Stark broadening of the D6 \rightarrow 2 Balmer line [14,15].

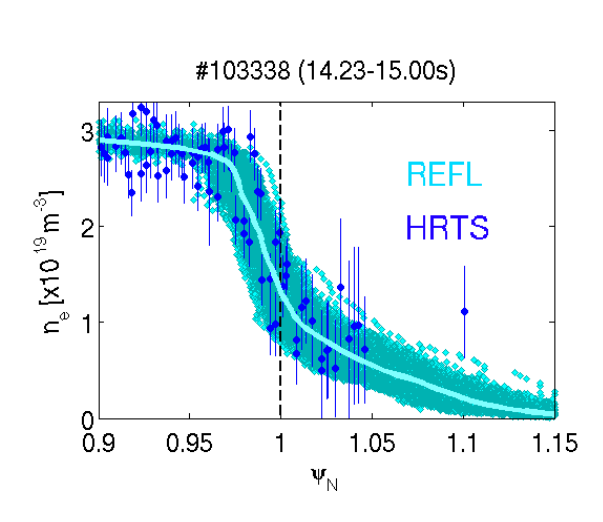
The upstream profiles are further classified in terms of the edge turbulence control parameter α_t [11] evaluated at the separatrix location (ψ_N =1). α_t describes the relative importance of drift wave transport (dominant for α_t << 1) and interchange turbulence transport (dominant for α_t >~ 1) at the plasma boundary, but noting that the transition between the two regimes is gradual. Recent studies have shown correlations between the power width (λ_q) in the near-SOL and α_t [11,16,17]. Also, with increasing α_t a broadening of the upstream density profiles in the far-SOL together with the formation of a density shoulder has been observed during gas puff scans on TCV and ASDEX-U [16,18] and triangularity scans on TCV [17]. This phenomenon is associated with an enhanced filamentary transport dominating the radial turbulent transport in the far-SOL and has been shown to result in a (undesirable) redistribution of the plasma wall heat loads with incresing α_t , away from the divertor targets towards the main chamber wall [18,19].

The main aim of the current work is to examine what role the α_t parameter plays on the JET tokamak for far-SOL density profile flattening. Beyond scans in gas puffing and triangularity, as in the TCV and ASDEX-U works mentioned above, additional comparisons are presented (impact of connection length to the divertor, divertor geometry, or pellet fuelling). The results obtained are described in the following sections.

2. IMPACT OF GAS PUFFING

Figure 3 shows the detailed edge electron density profile evolution obtained for the gas fuelling ramp example of figure 1. While in the confined region the density pedestal gradually drifts outwards and steepens, the SOL density steadily increases and effectively 'eats into' the height of the density pedestal. During this process, two things happen: a) α_t increases as a result of $n_{e,sep}$ increasing and $T_{e,sep}$ (not shown here) decreasing; and b) the SOL density gradually flattens (the extracted density decay lengths, $\lambda_{n,far}$, will be shown further below). This correlation is qualitatively in line with the observations reported on other devices. Also, as α_t values in excess of

unity are reached, a density shoulder with outer inflection radius beyond $\psi_N \sim 1.1$ becomes clearly visible. (The physics of what sets this outer inflection radius will be the focus of attention of the last section.)



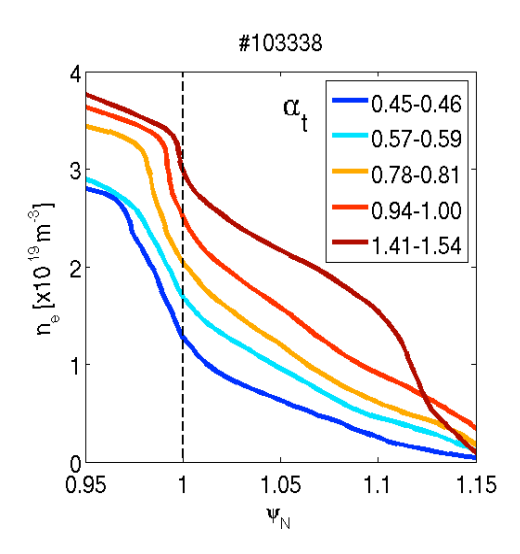


FIG. 2. Example of average (pre-ELM) reflectometry density profile determination (light cyan, solid line) for one subinterval of the fuelling ramp in figure 1. The average is done over (several hundred) individual reflectometry profiles (dark cyan diamonds). HRTS datapoints (blue circles) are also shown, for comparison.

FIG. 3. Sequence of average pre-ELM edge density profiles obtained for different stages (sub-intervals) of the fuelling ramp in figure 1 (gas puffing). The legend gives the inferred α_t values for each density profile.

3. IMPACT OF PELLET FUELLING

In some pulses, the fuelling ramps up to the H-L backtransition were done with pellets, not gas. The latter were implemented by gradually ramping up the pellet frequency, at fixed pellet size. For pellet fueling to be suffi-

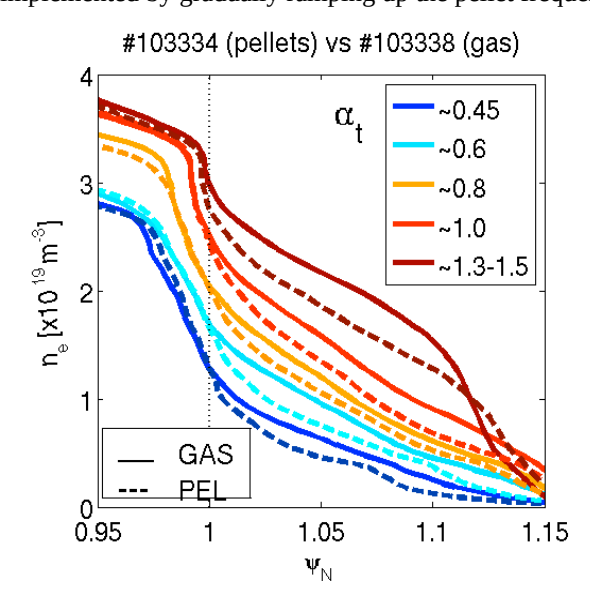


FIG. 4. Gas puff vs pellet fuelling comparison of average pre-ELM edge density profiles for two fuelling ramps up to the H-L backtransition. Same colours are used for profiles with approximately matched α_i .

cient, the divertor cryopumps were operated at liquid N₂ temperature (and also for the gas references, for direct comparability). Figure 4 compares the edge density profiles obtained for a pair of gas or pellet fuelled -but otherwise identical- discharges. The main difference found is that switching from gas fuelling to pellet fuelling yields systematically lower absolute densities both in the near- and the far- SOL regions (but not for the separatrix density itself). The figure shows that this is true not only when comparing profiles with matched α_t , but also for profiles with matched separatrix density (n_{e,sep}). However, most of this difference originates from the near-SOL, where the profiles diverge $(\lambda_{n,near}$ steeper with pellets than with gas), whereas the radial decay in the far-SOL is found to be comparable with pellets or gas. Furthermore, the figure shows that SOL density shoulders can also develop with pellet fuelling. Similar thresholds for density shoulder formation in terms of turbulence control parameter α_t have been found with pellets or gas ($\alpha_t > \sim 1.2$). However, the density shoulder found for the pellet case is less pronounced (lower absolute height compared to gas).

4. IMPACT OF PLASMA TRIANGULARITY

Since ITER is designed to operate at high triangularity ($<\delta>\sim$ 0.5), it is important to understand how triangularity influences the far-SOL density. Figure 5 shows the sequence of edge density profiles obtained by repeating a fuelling ramp at two different triangularities. This was mainly accomplished by increasing the upper triangularity by \sim 50%, while the lower triangularity was kept similar to preserve the strike point geometry in the divertor (for which there will be a separate comparison, see below). It is noted that this range of triangularity variation is smaller than the one presented in [17]. The figure shows that for a given α_t (i.e. similar line colours in dashed or solid), the densities in the far-SOL tend to be slightly higher with increased triangularity (at least up to $\psi_N \sim 1.1$) but overall this difference is modest. The main difference found is that the increased plasma triangularity enables access to higher absolute edge densities (both for pedestal and SOL), including a higher density shoulder. Note in particular that for the highest density (grey solid line) profile in figure 3, no low triangularity (grey dashed line) counterpart exists, because at low triangularity the H-L backtransition (HDL) already took place at lower density.

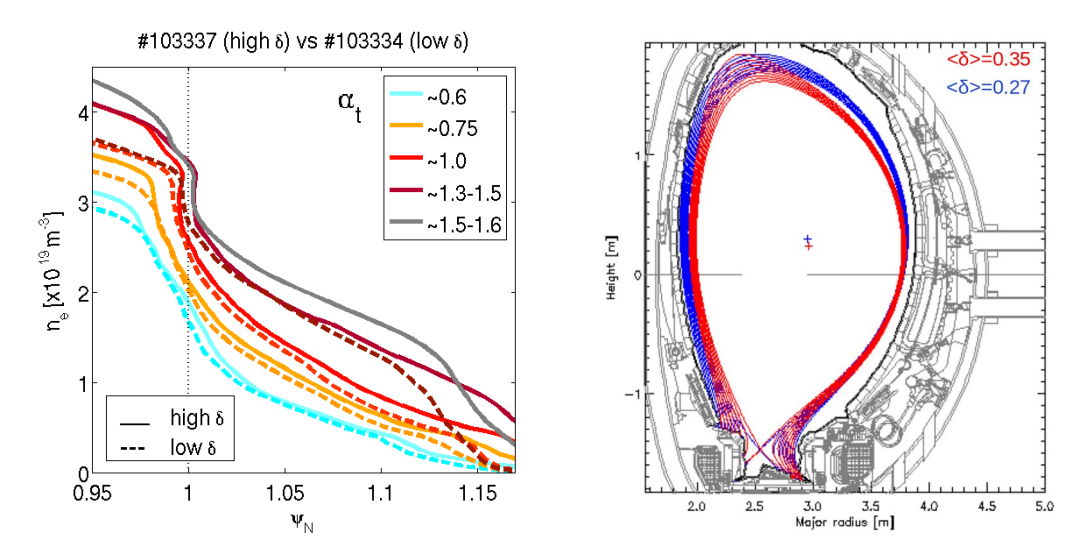


FIG. 5. Sequence of inter-ELM averaged edge density profiles obtained during different phases of a fuelling ramp for two discharges with different triangularity (the respective plasma shapes are shown on the right, together with their average triangularities). Same profile colours are used for profiles with approximately matched α_n .

5. IMPACT OF PLASMA CURRENT (AT FIXED TOROIDAL FIELD)

Increasing plasma current at fixed toroidal magnetic field has two major consequences: Firstly, since the H-mode density limit is widely accepted to be the result of an edge density (separatrix) limit, and empirically this limit is found to scale approximately with the Greenwald density, higher I_p enables access to higher absolute separatrix densities. Secondly, by keeping B_{tor} fixed, the edge safety factor reduces and hence the parallel connection length between the outer midplane and the outer divertor target (L_{\parallel}) becomes shorter with increasing I_p . Figure 6 shows the edge density profiles obtained for a pair of discharges in which the fuelling ramp was applied at two levels of I_p (1.3MA and 1.9MA) up to the H-L backtransition. Correspondingly, L_{\parallel} decreases by about 1/3 between the low and high I_p cases (the values of L_{\parallel} are also indicated). It can be seen that the edge density profiles clearly evolve very differently with increasing edge density. Note that the range of α_t values obtained during the fuelling ramp is also different. The most striking difference is the absence of density shoulder formation at the highest densities when repeating the same fuelling ramp at increased I_p (lower L_{\parallel}). This is qualitatively consistent with results obtained with L-mode plasmas on TCV and ASDEX-U [20]. In particular, it was reported there that, when reducing I_p at constant toroidal field, the scrape-off layer profiles tend to develop a clear density shoulder at a lower edge density.

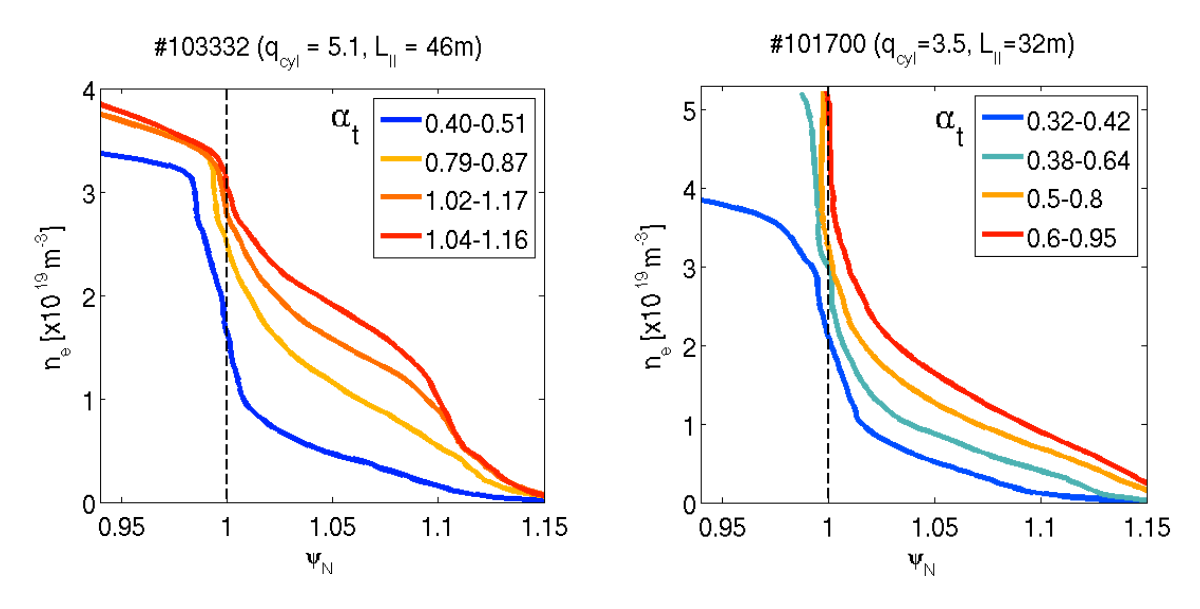


FIG. 6. Density profile evolution during fuelling ramp up to H-L backtransition, at low plasma current =1.3MA (left), and with I_p increased to 1.9MA at fixed B_{tor} (right).

6. ROLE OF DIVERTOR GEOMETRY

It is well known that by changing the outer strike point (OSP) geometry from horizontal target (HT) to vertical target (VT), the neutral pathways, recycling patterns and ionisation source profiles in the divertor get modified [21]. As a result, divertor conditions will be different. This will include changes to the outer target electron densities ($n_{e,OT}$) and temperatures ($T_{e,OT}$) near the OSP and outer target collisionalities. The latter is a particularly interesting quantity for the main chamber far-SOL assessment, since it governs the electrical disconnection of the filaments from the divertor [22]. The left subplot in figure 7 shows the timetraces of the (spectroscopically inferred) ratio $n_{e,OT}/T_{e,OT}^2$ (as a proxy for collisionality) for a pair of low triangularity discharges with OSP locations either on VT or HT, in which the same fuelling ramp was applied. (The detailed divertor geometries for these two pulses are also shown further below, in figure 9). It can be seen that the divertor collisionalities are one to two orders of magnitude higher for the VT case than for HT, except towards the very end of the fuelling ramp (near H-L backtransition) where both collisionalities converge. The right subplot in figure 7 shows the cor-

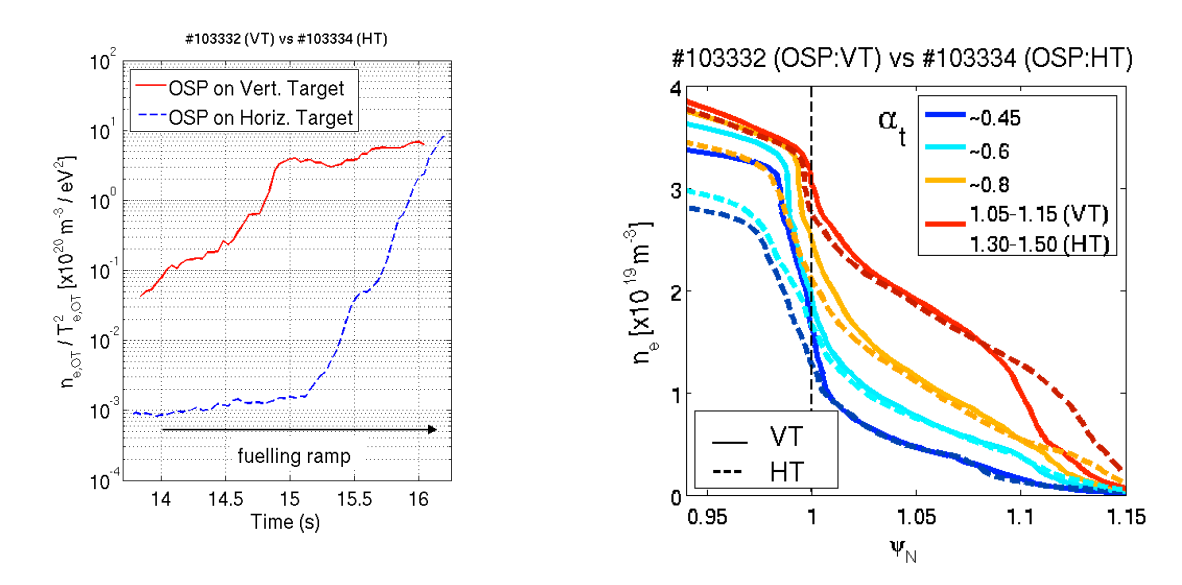
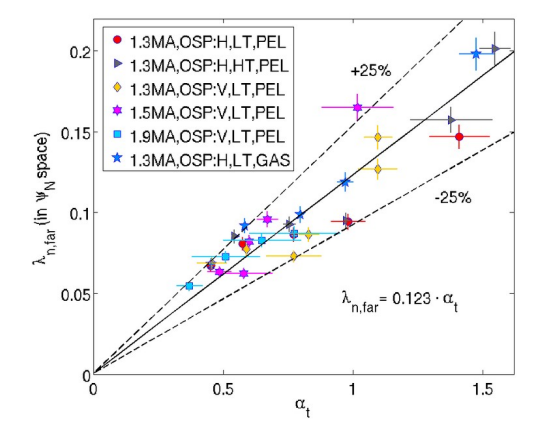


FIG. 7. Fuelling ramp for a pair of discharges with OSP on vertical target (solid) or horizontal target (dashed). Left: Time traces of spectroscopically inferred divertor collisionality ($\sim n_e/T_e^2$) near the OSP. Right: Comparison of inter-ELM averaged edge density profiles during different phases of the fuelling ramp, at approximately matched α_t .

responding sequence of edge density profiles obtained for the two discharges, again comparing profile pairs at similar α_t . A clear difference found is that for the profiles with α_t values < 1, the density profiles in the pedestal, separatrix and near-SOL regions are found to be systematically steeper in VT configuration than in HT. Also, in contrast to the previous direct comparisons shown above, ie. pellet vs gas fuelling (figure 4), or high vs low triangularity (figure 5), where matching α_t also resulted in similar $n_{e,sep}$ values, here we find that α_t and $n_{e,sep}$ are more decoupled. Remarkably, the figure also shows that moving further out into the far-SOL region these profile differences largely disappear, and the absolute densities and slopes are found to align well for profiles with similar α_t . Thus, the divertor geometry of the outer strike point (OSP) is NOT found to impact the radial decay in the far-SOL ($\psi_N > \sim 1.025$) for given α_t , even though the two cases have radically different divertor collisionalities. Figure 7 also demonstrates very explicitly that $\lambda_{n,far}$ and $\lambda_{n,near}$ are set via independent mechanisms, and that the two are uncorrelated, as reported previously (e.g. [23]). For α_t values > 1, density shoulders are seen to form equally, both in VT and HT. The maximum shoulder height reached just before the H-L backtransition is very similar in VT and HT, even though the inferred values for α_t were not perfectly matched here.

7. RADIAL DENSITY DECAY IN THE FAR-SOL

Replotting the measured radial density profiles in log-linear coordinates generally shows the faster exponential decay in the near-SOL transits into a slower exponential decay in the far-SOL, typically beyond $\psi_N > 1.01$ -1.025. We formulate the latter as $\exp(-x/\lambda_{n,far})$, with $\lambda_{n,far}$ the radial density decay length in the far-SOL. $\lambda_{n,far}$ has been extracted for the entire profile dataset through fits over the relevant radial range (typically $\psi_N \sim 1.02-1.08$) in two ways: using as radial coordinate 'x' either the poloidal flux (ψ_N) or the 'real space' outer midplane radius (R_{mid}) . The outcome of this analysis is shown in figure 8, plotted against α_t . In both cases, a linear correlation between $\lambda_{n,far}$ and α_t is found over the entire density range. Perhaps the most important result of this work is that, in spite of the dataset's heterogeneity, the turbulence control parameter α_t evaluated at the separatrix position unifies the measured radial density decay length data in the far-SOL. This result identifies α_t as a good descriptor to quantify far-SOL density flattening on JET. It supports and further expands (to larger tokamak size and for a broad range of conditions) previous findings obtained on other medium-sized machines [16-18] that also indicated that the SOL density flattening is set by the balance between drift wave transport and interchange transport. Note also that the identification of α_t as the primary driver for SOL density flattening on JET also provides a straightforward explanation for the absence of density shoulder formation for the Ip=1.9MA case (cyan squares in figure 8), namely that the q_{cyl} reduction from 5.1 to 3.5 effectively prevents α_t ($\sim q_{cyl}^2$) from exceeding unity during the whole density ramp.



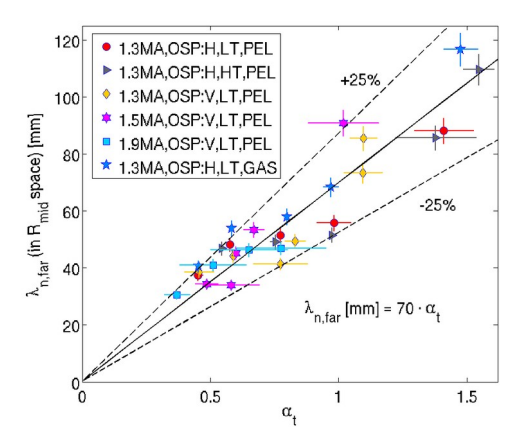


FIG. 8. Radial density decay in the far-SOL ($\lambda_{n,far}$) as a function of turbulence control parameter α_i , for the full dataset of discharges. Left: computing the density decay in equilibrium space (normalised poloidal flux, unitless). Right: computing the density decay in real space (outer midplane, mm). The legend provides additional information for each scenario (I_p , whether OSP on horizontal or vertical, low or high triangularity, fuelling method). The formula for the obtained least-squares linear fit (solid line) is also given.

8. DENSITY SHOULDER'S OUTER INFLECTION RADIUS

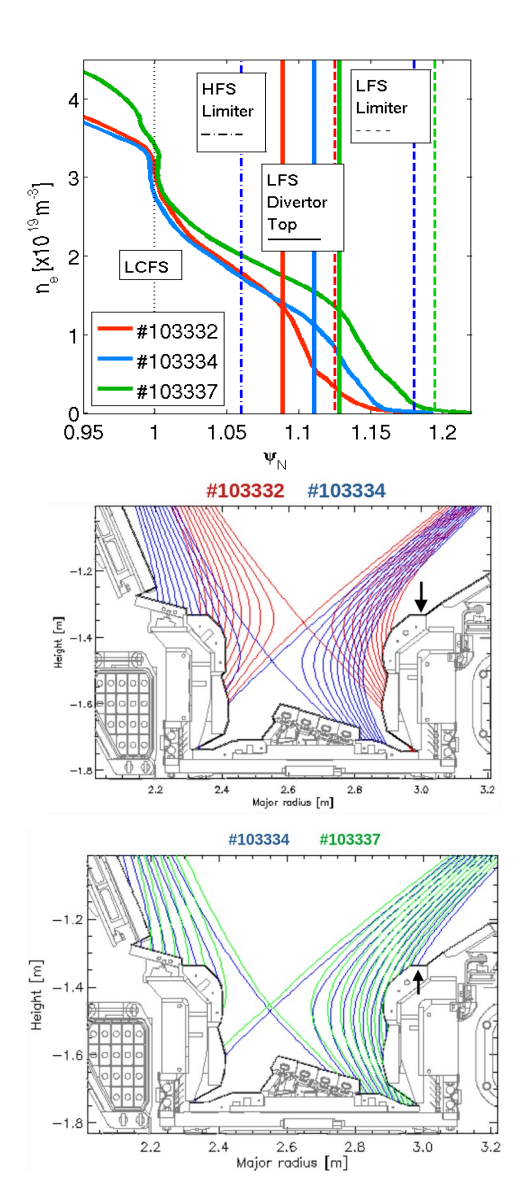


FIG. 9. (Top): SOL density shoulders obtained with three different plasma shapes, showing different outer inflection radii. The vertical lines (same colour convention as the profiles) mark the intersection radii with different wall elements. (Middle and Bottom): Divertor geometry for the three pulses. The black arrow marks the location corresponding to 'LFS Divertor Top'.

To correctly estimate how high dense the plasma arriving right in front of the main chamber tiles in ITER will be, it is also crucial to understand what sets the radius of the outer inflection of the density shoulder and whether it is possible to control it by external means. Previous studies on ASDEX-U [24,25] found that the outer inflection radius was set by the nearest intersection of flux surfaces with the LFS poloidal limiters. The JET density ramp experiments described here were run with a higher than usual clearance to the outer wall for operational reasons. Figure 9 (top) shows three examples of density profiles exhibiting density shoulders with different outer inflection radii. These were obtained in three separate discharges with different plasma shapes. In all three cases, flux surface mapping shows the nearest interaction with the LFS limiters takes place well beyond the shoulder inflection radius. Therefore, in these shots the outer inflection radius is not set by the LFS limiters. A similar exercise for the inner wall HFS limiter (anyway unlikely to be important for outwards ballooning LFS filaments) shows the closest HFS location is too far inboard, hence can also not explain the shoulder inflection. Instead, the best correlation is found between the shoulder inflection radius and the intersection of flux lines with the LFS divertor top (shown by the black arrow in divertor flux subplots of figure 9). A possible explanation for this is that while filaments will be electrically disconnected from the dense and cold divertor, electrical connection might be restored in the hotter and less dense region just outside of the divertor. This important finding may provide a route to prevent direct contact of a density shoulder in ITER with the main chamber walls. Namely, through careful equilibrium design, the first filament 'contact point' could be moved to a more a suitable location in the divertor vicinity.

9. CONCLUSIONS

FM-CW reflectometry profiles have been carefully evaluated in conjunction with TS and far-IR interferometry for a set of H-mode density ramp experiments covering a variety of conditions (different plasma triangularity, vertical vs horizontal outer target geometry, different parallel connection lengths to the divertor L_{\parallel} , or exchanging gas fuelling against pellets). When comparing the edge n_e profiles at constant α_t , in terms of *absolute* electron densities in the far-SOL the differences found are mainly originating from further inwards (near-SOL, separatrix and pedestal regions). Most importantly, α_t is found to unify the *radial decay* of n_e in the far-SOL for the entire dataset, typically to within +- 25%. A direct propor-

tionality is found between the measured density decay length in the far-SOL and α_t , both in flux coordinates $(\lambda_{n,far} [\psi_N] = 0.123 * \alpha_t)$ and in real space $(\lambda_{n,far} [mm] = 70 * \alpha_t)$. The *inner* inflection point marking the transition between near- and far-SOL regions has been consistently found to be in the range $\psi_N \sim 1.01\text{-}1.025$, while the *outer* inflection of the density shoulders seen to develop at high enough α_t (>~ 1.2) appears to be set by the intersection with the LFS divertor top. These findings offer a pathway to estimate with higher confidence how high dense the plasma arriving right in front of the main chamber tiles in ITER will be. Future work to enable effective interpolation to ITER should include comparison and combination with data from smaller or medium size tokamaks, in order to identify machine size dependencies.

ACKNOWLEDGEMENTS

This scientific paper has been published as part of the international project co-financed by the Polish Ministry of Science and Higher Education within the programme called 'PMW' for 2023–2025. This work has been carried out within the framework of the EUROfusion Consortium, funded by the European Union via the Euratom Research and Training Programme (Grant Agreement No 101052200 — EUROfusion). Views and opinions expressed are however those of the author(s) only and do not necessarily reflect those of the European Union or the European Commission. Neither the European Union nor the European Commission can be held responsible for them.

REFERENCES

- [1] Barabaschi, P. et al Fus. Eng. Des. 215 (2025) 114990 https://doi.org/10.1016/j.fusengdes.2025.114990
- [2] Loarte, A. et al Plasma Phys. Control. Fusion 67 (2025) 065023 https://doi.org/10.1088/1361-6587/add9c9
- [3] Romazanov, J. et al Nucl. Fusion 62 (2022) 036011 https://doi.org/10.1088/1741-4326/ac4776
- [4] Eksaeva, A. et al Phys. Scr. 97 (2022) 014001 https://doi.org/10.1088/1402-4896/ac454f
- [5] Carralero, D. et al Nucl. Fusion 54 (2014) 123005 http://dx.doi.org/10.1088/0029-5515/54/12/123005
- [6] Morales, R.B. et al Rev. Sci. Instrum. 95 (2024) 043501 https://doi.org/10.1063/5.0176696
- [7] Braithwaite, G. et al Rev. Sci. Instrum. 60 (1989) 2825 https://doi.org/10.1063/1.1140666
- [8] Boboc, A. et al Rev. Sci. Instrum. 83 (2012) 10E341 https://doi.org/10.1063/1.4737420
- [9] Pasqualotto, R. et al Rev. Sci. Instrum. 75 (2004) 3891 https://doi.org/10.1063/1.1787922
- [10] Frassinetti, L. et al Rev. Sci. Instrum. 83 (2012) 013506 http://dx.doi.org/10.1063/1.3673467
- [11] T. Eich et al Nucl. Fusion 60 (2020) 056016 https://doi.org/10.1088/1741-4326/ab7a66
- [12] Lomanowski, B.A. et al Plasma Phys. Control. Fusion 62 (2020) 065006 https://doi.org/10.1088/1361-6587/ab7432
- [13] Lumma, D., Terry, J.L., Lipschultz, B., Phys. Plasmas 4 (1997) 2555 https://doi.org/10.1063/1.872234
- [14] A.G. Meigs et al J. Nucl. Mat. 438 (2013) S607 http://dx.doi.org/10.1016/j.jnucmat.2013.01.127
- [15] B Lomanowski et al Nucl. Fusion 55 (2015) 123028 http://dx.doi.org/10.1088/0029-5515/55/12/123028
- [16] A. Stagni et al Nucl. Fusion 62 (2022) 096031 https://doi.org/10.1088/1741-4326/ac8234
- [17] A. Stagni et al Nucl. Fusion **64** (2024) 026016 https://doi.org/10.1088/1741-4326/ad1a56
- [18] A. Redl et al Nucl. Fusion 64 (2024) 086064 https://doi.org/10.1088/1741-4326/ad5457
- [19] A. Redl et al Nucl. Mat. Energy 34 (2023) 101319 https://doi.org/10.1016/j.nme.2022.101319
- [20] N. Vianello et al Nucl. Fusion 60 (2020) 016001 https://doi.org/10.1088/1741-4326/ab423e
- [21] D. Moulton et al Nucl. Fusion 58 (2018) 096029 https://doi.org/10.1088/1741-4326/aacf0f
- [22] Myra, J.R., Russell, D.A., D'Ippolito, D.A., Phys. Plasmas 13 (2006) 112502 https://doi.org/10.1063/1.2364858
- [23] Carralero, D. et al Nucl. Mat. Energy 12 (2017) 1189 http://dx.doi.org/10.1016/j.nme.2016.11.016
- [24] Bernert, M., 'Analysis of the H-mode density limit in the ASDEX Upgrade tokamak using bolometry', PhD thesis, LMU Muenchen (2013) http://edoc.ub.uni-muenchen.de/16262/, pages 51/52.
- [25] Tal, B. et al Nucl. Fusion **64** (2024) 126063 https://doi.org/10.1088/1741-4326/ad8362